Structural and Magnetic Studies of Ordered Oxygen-Deficient Perovskites *Ln*BaCo$_2$O$_{5+\delta}$, Closely Related to the "112" Structure

A. Maignan,[1] C. Martin, D. Pelloquin, N. Nguyen, and B. Raveau

Laboratoire CRISMAT, UMR 6508 associée au CNRS, ISMRA and Université de Caen, 6 Boulevard du Maréchal Juin, 14050, Caen Cedex, France

The system *Ln*BaCo$_2$O$_{5+\delta}$, related to the "112" type structure ($a_p \times a_p \times 2a_p$), has been studied for *Ln* = Pr, Nd, Sm, Eu, Gd, Tb, Dy, and Ho, with various oxygen stoichiometries. According to the size of the lanthanide and to the oxygen stoichiometry, two kinds of supercells, $a_p \times 2a_p \times 2a_p$ and $3a_p \times 3a_p \times 2a_p$, arising from different orderings between oxygen and vacancies in the [*Ln*O$_\delta$] layer, have been evidenced by electron diffraction and HREM techniques. The influence of the oxygen content on the metal–insulator transition and the corresponding magnetic susceptibility anomaly is studied. Magnetoresistant (MR) effects are observed for all of the as-synthesized samples and are very sensitive to the oxygen content. They are related to strong competitions between ferromagnetism and antiferromagnetism: the $\chi'(T)$ curves exhibit a cusp at T_{cusp} which coincides approximately with T_{MR}, the appearance of the MR. © 1999 Academic Press

INTRODUCTION

The recent studies of manganese oxides have opened the route to the exploration of oxides whose colossal magnetoresistance (CMR) properties are most fascinating. In addition to the manganites, the cobalt oxides La$_{1-x}$Sr$_x$CoO$_3$ are of great interest owing to their magnetoresistance properties, although they exhibit a small resistance ratio, $R_0/R_H \approx 2$ in a magnetic field of 6 T (1–3). These oxides have in common one structural feature: their structure derives from the ideal perovskite. The existence of ordered oxygen-deficient perovskites *Ln*BaCo$_{2-x}$M$_x$O$_{5+\delta}$ with interesting magnetic properties (4) has stimulated the research of pure cobalt compounds. This investigation has led to the discovery of giant magnetoresistance properties in *Ln*BaCo$_2$O$_{5+\delta}$ oxygen-deficient perovskites for *Ln* = Eu and Gd (5). The resistance ratios of these materials, higher than 10, are the highest that have been observed to date in the cobalt-based perovskites.

The oxygen-deficient perovskites *Ln*BaCo$_2$O$_{5+\delta}$ derive from the "112" type structure YBaFeCuO$_5$ (6), so that for

$\delta = 0$ their structure consists of double-pyramidal cobalt layers containing the barium cations, interleaved with lanthanide layers. In fact, the magnetic properties of these oxides are very sensitive to the oxygen stoichiometry. Moreover, the influence of the structure on these properties is complicated by the complex crystal chemistry of these phases, which show various superstructures as δ varies. This paper deals with the systematic study of the structure and magnetotransport properties of the whole series of oxides *Ln*BaCo$_2$O$_{5+\delta}$, with *Ln* = Pr, Nd, Sm, Eu, Gd, Tb, Dy, and Ho. It shows the important influence of the oxygen stoichiometry on those properties and the close correlations between the magnetoresistance effect and the competition that appears between ferromagnetism and antiferromagnetism in these materials.

EXPERIMENTAL

All of the samples were prepared under exactly the same conditions: by solid state reaction of *Ln*$_2$O$_3$, BaCO$_3$, and Co$_3$O$_4$, weighted in stoichiometric proportions. After decarbonation at 1000°C, the powders were pressed into bars, heated for 24 h in air at 1100°C, and slowly cooled to room temperature.

The purity of the compounds was checked by X-ray diffraction. The powder X-ray patterns were recorded by using a Philips diffractometer with Cu*K*α radiation. The data were collected at room temperature by step scanning (0.02° by step) over the angular range $10° \leq 2\theta \leq 120°$ and analyzed with the program Fullprof (7).

The oxygen content was determined by iodometric titration and, for *Ln* = Pr, Gd, and Ho, by thermogravimetric analysis (at 1100°C under an Ar flow).

The samples were checked by electron diffraction (ED) using a JEOL 200Cx electron microscope fitted with a eucentric goniometer ($\pm 60°$) and equipped with an EDX analyzer. The high-resolution electron microscopy (HREM) was performed with a JEOL 2010Cx and TOPCON 002B operating at 200 kV having a point resolution of 2.5 and

1.8 Å, respectively. HREM images were carried out with the Mac-Tempas multislice program.

The magnetotransport properties (four-probe method) were investigated by means of a physical property measuring system (PPMS), the ac susceptibility and magnetization from an ac–dc SQUID Quantum Design magnetometer ($h_{ac} = 3$ Oe). The high-temperature susceptibility was registered with a Faraday balance ($T_{max} \approx 800$ K).

RESULTS AND DISCUSSION

Structural Study

The synthesis in air, according to the experimental conditions, allows eight oxygen-deficient perovskites $LnBaCo_2O_{5+\delta}$ to be isolated for $Ln =$ Pr, Nd, Sm, Eu, Gd, Tb, Dy, and Ho. The iodometric titrations combined with TGA measurements show that as the size of the lanthanide decreases, the oxygen content decreases from $\delta \approx 0.7$ for $Ln =$ Pr and Nd to $\delta \approx 0.4$ for $Ln =$ Sm, Eu, Gd, and Tb to $\delta \approx 0.3$ for $Ln =$ Dy and Ho. The crystal data of these air-synthesized oxides, deduced from the X-ray diffraction (XRD) and electron diffraction (ED) studies, are listed in Table 1. All of the XRD patterns can be indexed using a tetragonal $a_p \times a_p \times 2a_p$ subcell characteristic of the "112" structure (a_p being the cell parameter of the cubic perovskite). However, the ED patterns of these phases show the existence of superstructures without conditions limiting the reflections. Two kinds of supercells are observed according to the size of the lanthanide. For larger lanthanides, i.e., from Pr to Tb, a doubling of one parameter is observed (see Fig. 1 for $Ln =$ Gd), corresponding to an $a_p \times 2a_p \times 2a_p$ supercell, whereas for smaller lanthanides, i.e., for Ho and Dy, a tripling of two parameters is obtained, leading to a $3a_p \times 3a_p \times 2a_p$ supercell (see Fig. 2 for $Ln =$ Ho),

similar to that reported in $YBaCo_2O_5$ annealed in pure oxygen (8).

Such a variation of the oxygen content and of the structure with the size of the lanthanide suggests a possible ordering between oxygen and vacancies in the lanthanide layer. Moreover, a variation of the oxygen stoichiometry can be considered by varying the experimental conditions during the synthesis, especially the oxygen pressure. Such a hypothesis is confirmed from the study of the Eu and Gd compounds (Table 2). The synthesis of the Eu phase in an argon flow at 1100°C leads to a significant decrease of the oxygen content, corresponding to the formula $EuBaCo_2O_5$ ($\delta = 0$); moreover, in this phase the superstructure along $\vec{b}$ has disappeared so that the actual cell becomes $a_p \times a_p \times 2a_p$. In the same way, annealing the air-prepared phase $GdBaCo_2O_{5.4}$ in an argon flow (at 850°C for 1.5 h, with slow cooling) leads to $GdBaCo_2O_5$ ($\delta = 0$), also characterized by an $a_p \times a_p \times 2a_p$ cell. The reversibility of the phenomenon is easily observed by annealing this Ar-annealed $GdBaCo_2O_5$ at 400°C for 48 h under an oxygen pressure of 100 bar. The oxygen enters into the lattice, leading to $GdBaCo_2O_{5.6}$ ($\delta = 0.6$), characterized by a superstructure along $\vec{b}$, i.e., by the $a_p \times 2a_p \times 2a_p$ supercell. In the same way, a similar annealing of the Ho sample $HoBaCo_2O_{5.3}$ under an oxygen pressure of 100 bar leads to $HoBaCo_2O_{5.5}$, and the $3a_p \times 3a_p \times 2a_p$ supercell is replaced by an $a_p \times 2a_p \times 2a_p$ supercell. Note that this last structural form is not stable under the electron beam and the $3a_p \times 3a_p \times 2a_p$ supercell reappears after several minutes of irradiation. In the same way the oxygen content of a Pr air-prepared sample is lowered to $O_{5.5}$ by annealing in a reducing atmosphere, without changing the $a_p \times 2a_p \times 2a_p$ structure.

From these results and those previously reported for $YBaCo_2O_{5+\delta}$ (8), it clearly appears that the ordering of the

TABLE 1
Structural Parameters (Lattice Parameters and Volume Are Given in the Primitive Cell $a_p \times a_p \times 2a_p$ to Compare the Values) and Physical Parameters from Resistivity and Susceptibility Curves for $LnBaCo_2O_{5+\delta}$ Phases with $Ln =$ Pr, Nd, Sm, Eu, Gd, Tb, Dy, and Ho

Parameter	Pr	Nd	Sm	Eu	Gd	Tb	Dy	Ho
a (Å) (a_p)	3.9019(1)	3.8969(1)	3.8862(1)	3.8834(1)	3.8747(1)	3.8667(1)	3.8763(1)	3.8734(1)
b (Å) (a_p)	3.9061(1)	3.9015(2)	3.9085(1)	3.9159(2)	2.9106(1)	3.9076(1)	3.8789(3)	3.8719(2)
c (Å) ($2a_p$)	7.6306(1)	7.6115(1)	7.5661(1)	7.5406(2)	7.5338(1)	7.5164(1)	7.5036(2)	7.4959(1)
V (Å^3)	116.30	115.72	114.92	114.67	114.15	113.57	112.82	112.42
$r_{Ln_{IX}}$ (Å) (12)	1.179	1.163	1.132	1.120	1.107	1.095	1.083	1.072
δ^a	0.7(0.7)	0.7	0.4	0.4	0.4(0.5)	0.4	0.3	0.3(0.4)
T_{MI}(K)			320	360	350	330	310	
ρ_{400K} (Ω cm)	4×10^{-4}	9×10^{-4}	9×10^{-4}	9×10^{-4}	1×10^{-3}	1.5×10^{-3}	1.5×10^{-3}	4×10^{-3}
T_{cusp} (K)	125	105	252	275	275	280		
$\chi'(T_{cusp})_{133Hz}$ (emu/g)	2.0×10^{-2}	1.1×10^{-2}	1.2×10^{-2}	6.0×10^{-3}	4.3×10^{-2}	2.5×10^{-2}	3.0×10^{-2}	1.0×10^{-3}
MR_{125K} (%)	16	20	9	20	22	8	5	4

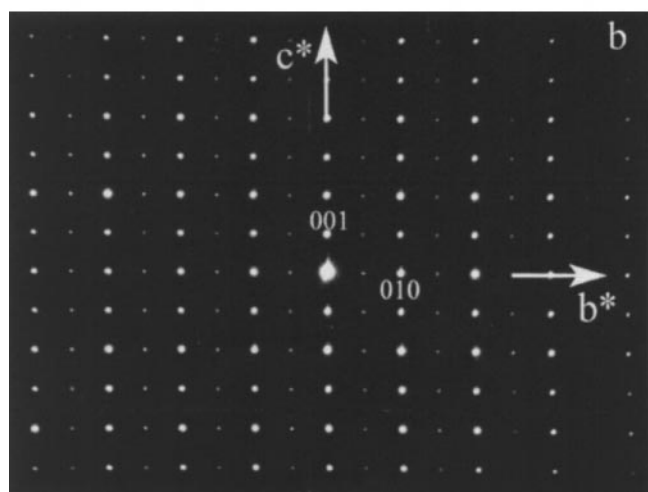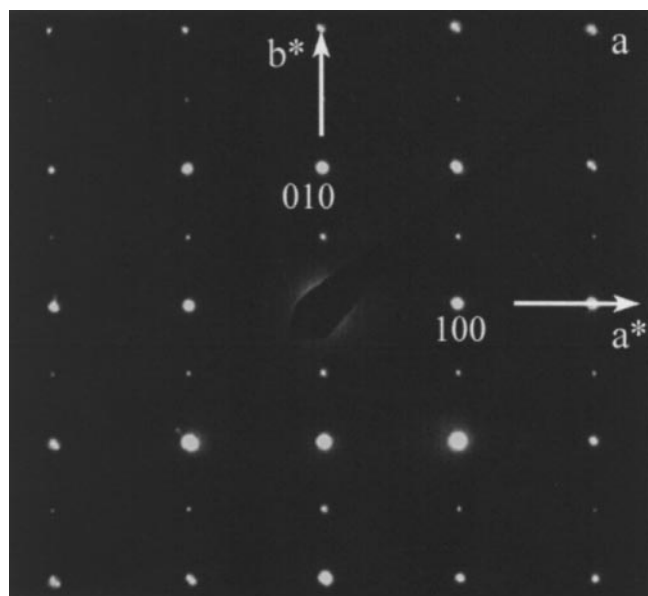^{a} Value determined by iodometric titration; values in parentheses determined by TGA.

FIG. 1. Electron diffraction (ED) patterns of air-synthesized GdBaCo$_2$O$_{5+\delta}$ oriented (a) [001] and (b) [100]. These patterns are indexed to the ideal "112" unit cell ($a_p \times a_p \times 2a_p$).

FIG. 2. Electron diffraction patterns of air-synthesized HoBaCo$_2$O$_{5+\delta}$ oriented (a) [001] and (b) [100]. These patterns are indexed to the ideal "112" unit cell ($a_p \times a_p \times 2a_p$).

oxygen vacancies in the perovskite matrix is responsible for the various superstructures observed in the ED patterns. Then, HREM investigations of the three types of compounds were performed to propose structural models to explain the different superlattices. The first one, which corresponds to the ideal 112 structure previously observed for YBaFeCuO$_5$ (6), can be proposed for the Ar-synthesized or Ar-annealed phases L*n*BaCo$_2$O$_5$ ($\delta = 0$), in agreement with the [100] HREM image recorded for the Ar-annealed GdBaCo$_2$O$_5$ (Fig. 3a). In this image, the cobalt positions are highlighted (black arrows). Along $\vec{c}$, the brightest dots, correlated to the [CoO$_2$]$_\infty$ layers, are spaced by about 4 and 3.5 Å alternatively. They are separated by two kinds of rows of gray dots, corresponding to [BaO]$_\infty$ and [Gd]$_\infty$ layers,
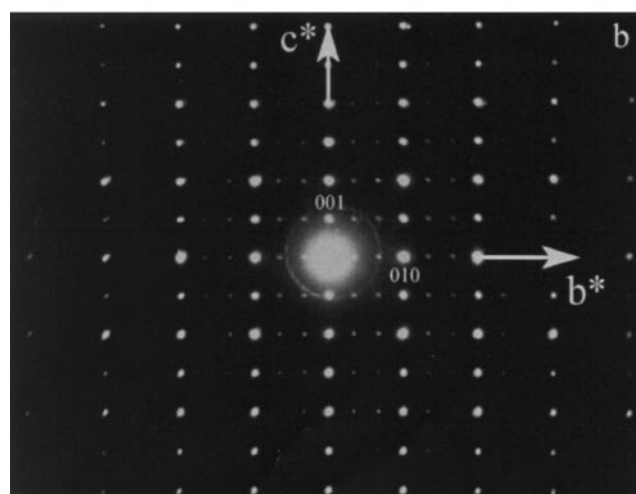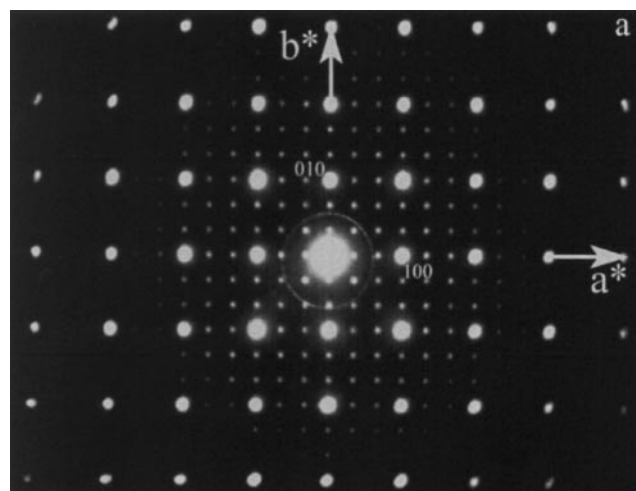
respectively. Such a contrast confirms the stacking sequence along $\vec{c}$: [BaO]–[CoO$_2$]–[Gd]–[CoO$_2$]–[BaO], characteristic of the 112 structure (Fig. 3b). This ideal structure,

TABLE 2
Evolution of the Structural Parameters for the Eu and Gd Compounds versus Oxygen Content

Compound	δ	a (Å)	b (Å)	c (Å)	V (Å^3)
Eu compound					
Air synthesized	0.4	3.8834(1)	2 × 3.9159(2)	7.5406(2)	229.34
Ar synthesized	0	3.9187(1)	3.9257(1)	7.5132(2)	115.58
O$_2$ synthesized	0.6	3.8795(1)	2 × 3.8994(1)	7.5665(2)	228.95
Gd compound					
Air synthesized	0.4	3.8750(1)	2 × 3.9106(1)	7.5345(1)	228.31
Ar annealed	0	3.9111(1)	3.9159(1)	7.5074(2)	115.73
P$_{O_2}$ annealed (after Ar annealed)	0.6	3.8729(1)	2 × 3.8774(1)	7.5566(2)	226.95

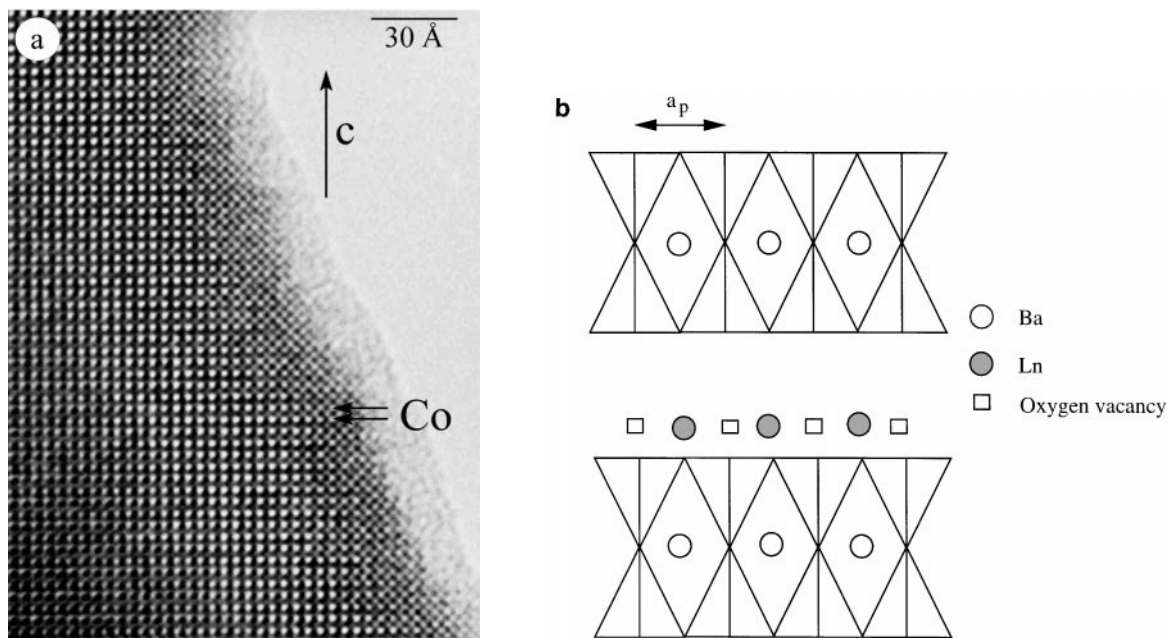**FIG. 3.** (a) [100] HREM image recorded for Ar-annealed $GdBaCo_2O_5$ and (b) corresponding structural model.

described by the stacking along $\vec{c}$ of double-pyramidal cobalt layers containing Ba^{2+} ions, i.e., with the formula $[BaCo_2O_5]_\infty$, interleaved with $[Ln]_\infty$, is indeed characterized by an $a_p \times a_p \times 2a_p$ actual cell. For the air-synthesized phase $GdBaCo_2O_{5.4}$, very similar [010] HREM images are observed whereas the [100] HREM images (Fig. 4a) show
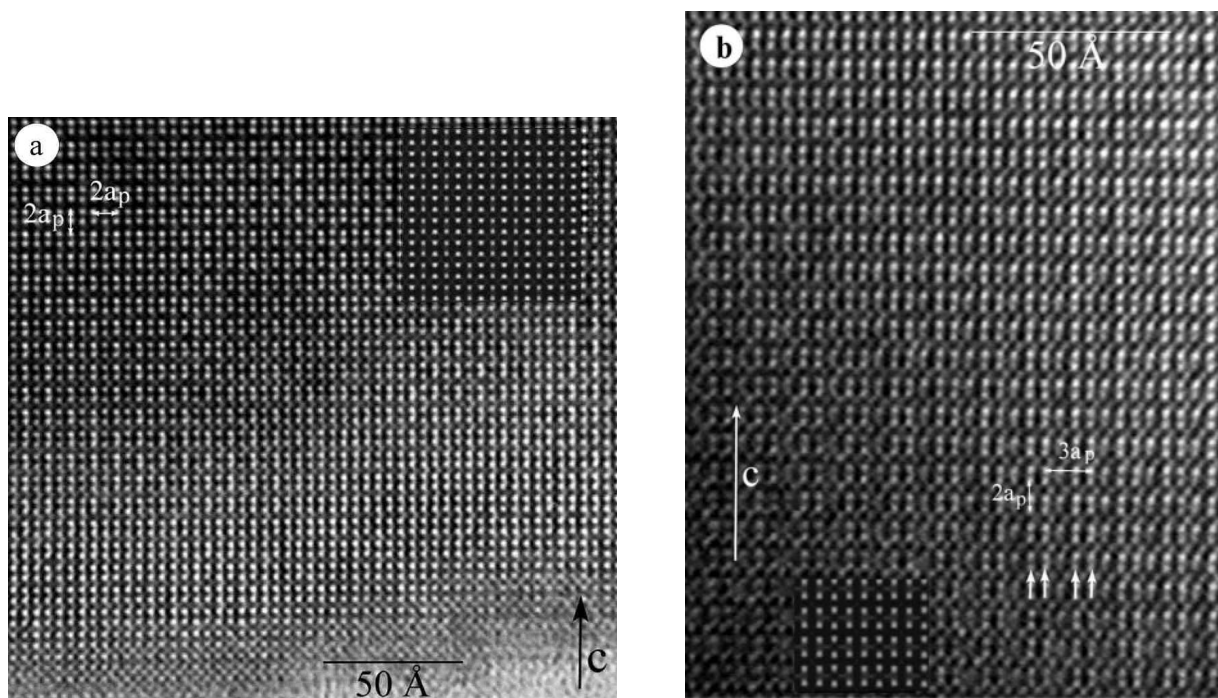

FIG. 4. [100] HREM images recorded for air-synthesized (a) $GdBaCo_2O_{5.4}$ and (b) $HoBaCo_2O_{5.3}$. Image simulations corresponding to a defocus value of -400 Å and a thickness of 80 Å, calculated from structural models presented in (d) and (e) (space group *Pmmm*), are pasted into the experimental images. (c) [001] HREM image recorded for air-synthesized $HoBaCo_2O_{5.3}$. The insets are the simulated image and ED pattern calculated from the structural model shown in (e) for a defocus value and a thickness close to 50 Å. Schematic oxygen distribution at the level of the lanthanide layer. (d) $a_p \times 2a_p \times 2a_p$ supercell: one row of oxygen out of two is occupied. (e) $3a_p \times 3a_p \times 2a_p$ supercell: two successive rows of vacancies alternate with one ordered oxygen-deficient row.
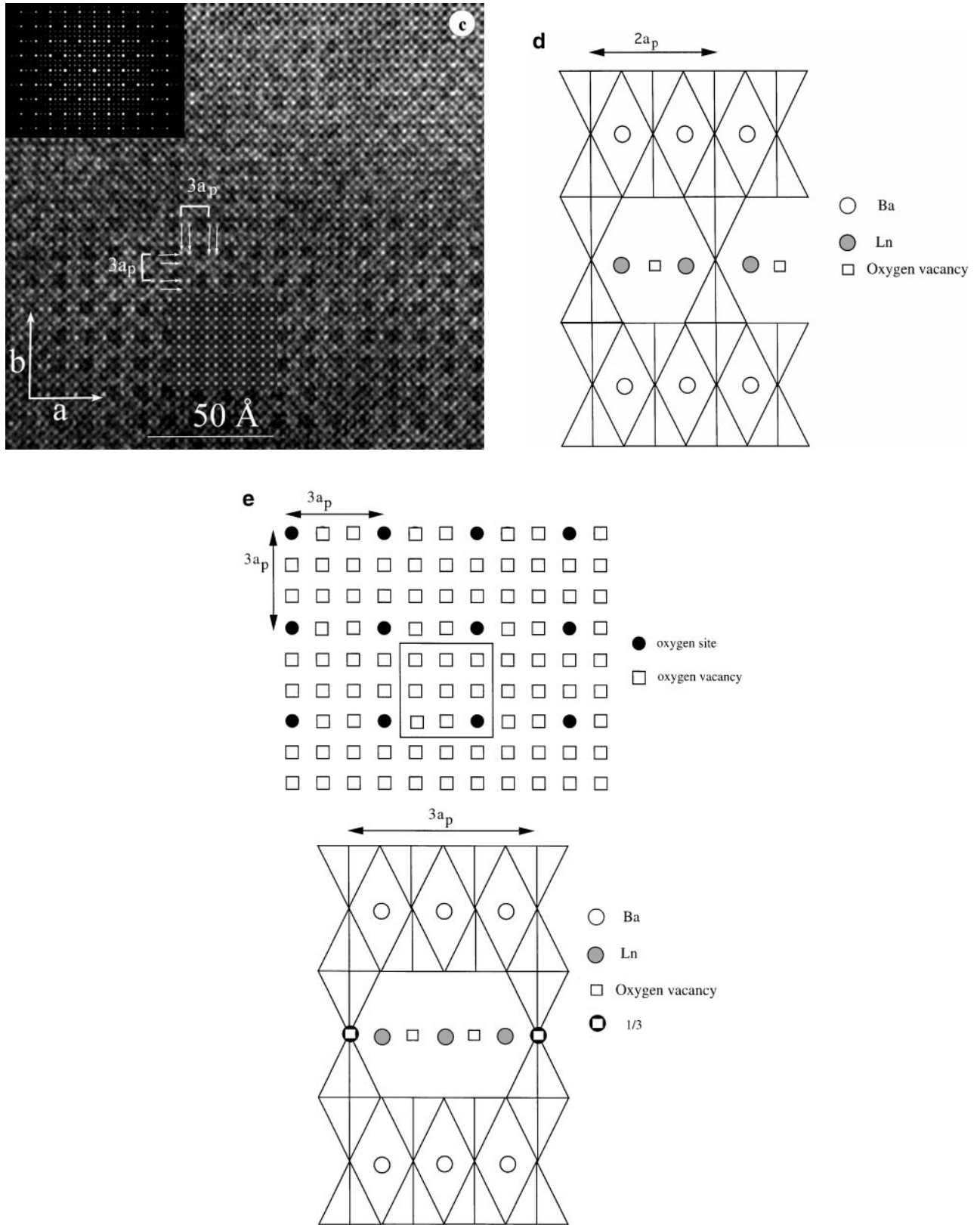
FIG. 4.—*Continued*

a very different contrast, generated by a doubling not only of the c parameter but also of the b parameter. At the level of the cobalt rows, one bright dot alternates indeed with one less bright dot along $\vec{b}$. In contrast, for the $LnBaCo_2O_{5.3}$ (Ln = Dy, Ho) phases, the [100] and [010] HREM images are identical. A typical image recorded for Ln = Ho is shown in Fig. 4b, where the cobalt rows are highlighted. A tripling of the a (or b) parameter can be distinguished as two bright dots (white arrows) which alternate with a darker one along $\vec{a}$ (or $\vec{b}$). These different contrast variations can be interpreted as an ordering between CoO_5 pyramids and CoO_6 octahedra. Thus for the $GdBaCo_2O_{5.4}$ phase, the alternating contrast can be associated with the following sequence along $\vec{b}$: Gd–O–Gd–□–Gd–O ... , which characterizes the oxygen–vacancy ordering within the $[GdO_\delta]_\infty$ layers (δ = 0.4). The stacking mode along $\vec{c}$ can be described as $[BaO]$–$[CoO_2]$–$[GdO_{0.4}]$–$[CoO_2]$–$[BaO]$, in agreement with the $a_p \times 2a_p \times 2a_p$ actual cell. Consequently, (010) octahedral cobalt layers $[CoO_3]_\infty$ alternate with $[CoO_{2.5}]_\infty$ pyramidal layers along $\vec{b}$. The structure of the air-synthesized phases $LnBaCo_2O_{5.4}$ (Ln = Sm, Eu, Gd, Tb) and of $HoBaCo_2O_{5.5}$ (PO_2 annealed), which exhibit a doubling of the b parameter, can then be deduced from the classical 112 structure by introducing one row of oxygen out of two at the level of the lanthanide layers (Fig. 4d). Such a structure may also exist for the air-synthesized compounds $PrBaCo_2O_{5.7}$ and $NdBaCo_2O_{5.7}$ and for the phase $GdBaCo_2O_{5.6}$ annealed under an oxygen pressure of 100 bar, the excess of oxygen with respect to the theoretical $O_{5.5}$ being statistically distributed in the pyramidal cobalt layers at the level of the Ln^{3+} cations. In the case of the $LnBaCo_2O_{5.3}$ (Ln = Dy, Ho) phases, the interpretation is more complex and one needs to examine the structure along the [001] direction (Fig. 4c). In this enlarged HREM image, the light dots are assimilated to cobalt positions. The tripling of the a and b parameters is clearly visible at the level of the cobalt rows, generated by a sequence of two bright dots (white arrows) separated by a gray one, with a periodicity of $3a_p$. This arrangement is consistent with the contrast variation previously observed along the [100] direction and can be interpreted as a sequence of two CoO_5 pyramids separated by one CoO_6 octahedron along both the $\vec{a}$ and $\vec{b}$ directions. From these observations, a structural model can be proposed for the distribution of the vacancies and oxygen atoms at the level of the LnO_δ layers: two successive rows of vacancies alternate with one ordered oxygen-deficient row (one oxygen for two vacancies) as shown in Fig. 4e. Such an ordering implies the theoretical stoichiometry $O_{5.11}$ instead of the experimental stoichiometry $O_{5.3}$ deduced from iodometric analysis. This suggests that the actual oxygen distribution at the level of the Ln layer is statistical except for one preferentially occupied site. Image simulations (inset in images of Fig. 4) calculated from theoretical models, described in Figs. 4d and 4e, have been performed. They fit

with the experimental images, showing the validity of the structural models.

A systematic neutron diffraction study of these oxides will be necessary to confirm these structural models. Powder X-ray diffraction data are indeed not sufficient to determine the oxygen positions with accuracy. It can be noticed that different orderings leading to a monoclinic distortion, especially among the [001] direction, can be locally observed, which disturb these characteristic contrasts. Moreover, many twinning phenomena are observed by HREM as illustrated for $GdBaCo_2O_{5.4}$, whose typical [001] ED pattern and HREM image are shown in Figs. 5a and 5b. From these images it can be seen that the interpretation of the experimental images, especially along [100], is disturbed by the softening of the contrast at the level of the $[GdO_{0.4}]_\infty$ layers, due to the superimposition of different 90° oriented domains.
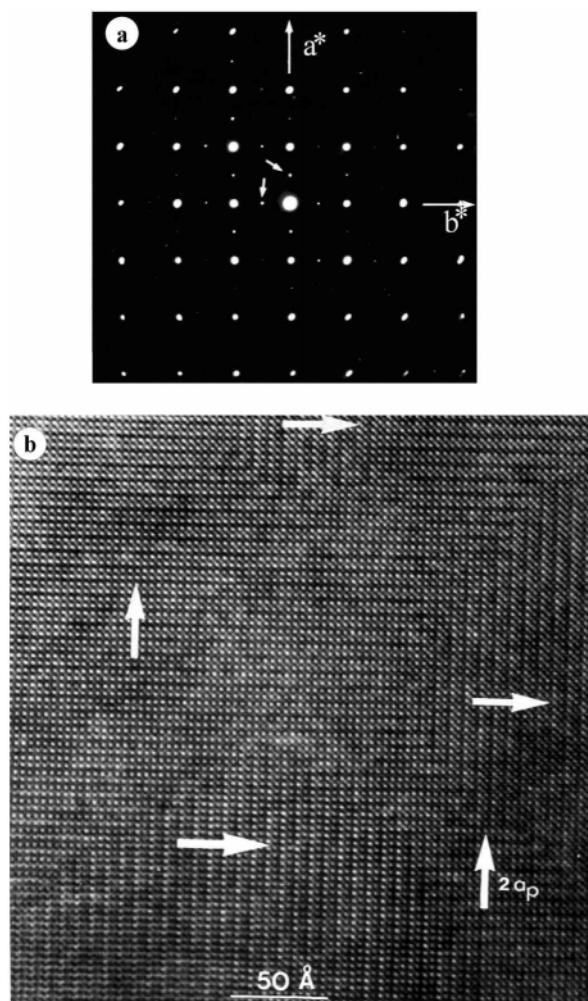
FIG. 5. (a) [001] ED pattern recorded for air-synthesized $GdBaCo_2O_{5.4}$ and (b) corresponding HREM image. 90° oriented domains are indicated by white arrows.
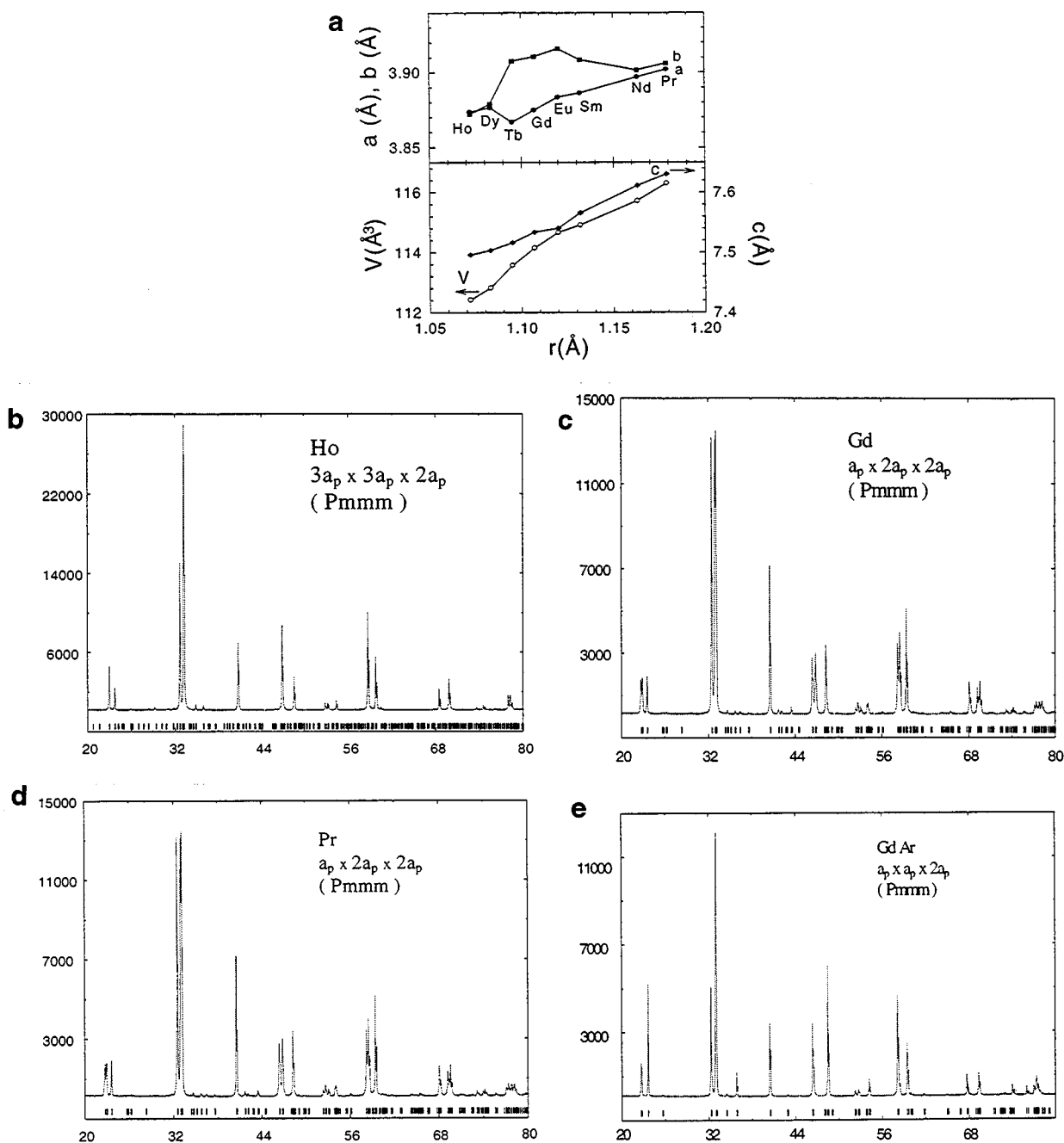
FIG. 6. (a) Unit cell parameters (a, b, c, and V) as a function of the Ln radius. XRD patterns of air-synthesized samples: (b) HoBaCo₂O₅₊δ, (c) GdBaCo₂O₅₊δ, (d) PrBaCo₂O₅₊δ, and (e) Ar-annealed Gd sample.

Considering the subcell parameters (Table 1), it is worth pointing out that, although the cell volume decreases with the size of the lanthanide cations, the distortion of the cell does not vary continuously. For the larger cations (Pr and Nd) and for the smaller ones (Dy and Ho), the subcell is pseudotetragonal. In contrast, for the intermediate-size cation (Sm, Eu, Gd, and Tb), a much larger orthorhombic distortion is observed. This distortion is evidenced by the graph of the lattice parameters versus the cationic radius (Fig. 6a) and by typical XRD patterns of air-synthesized samples (Figs. 6b–d) and the Ar-annealed Gd sample (Fig. 6e). In fact, it is closely related to the oxygen stoichiometry as shown for the O₅ Gd and Eu phases, which are much distorted compared to the LnBaCo₂O₅.₄ compounds (Table 2).

Metal–Insulator Transition: Influence of the Oxygen Stoichiometry

In a recent letter (5) we showed the magnetoresistance properties of the air-synthesized phases $EuBaCo_2O_{5.4}$ and $GdBaCo_2O_{5.4}$. A metal–insulator (MI) transition was evidenced at $T_{MI} \sim 360$ K, separating a nearly constant ρ region from an insulating region below 360 K. The $\rho(T)$ curves of the air-synthesized cobaltites $LnBaCo_2O_{5+\delta}$, registered on cooling from 400 K, are displayed in Fig. 7. One observes that the MI transition only appears for the intermediate lanthanides, i.e., $Ln = $ Sm to Dy. For the larger lanthanides ($Ln = $ Pr, Nd), a semimetallic behavior is observed in the 100–400 K temperature range, whereas for the smaller lanthanide ($Ln = $ Ho) a semiconducting-like behavior is observed. Moreover, it is worth pointing out that T_{MI} decreases smoothly with the size of the lanthanide from 350–360 K for $Ln = $ Gd and Eu to 330 K for $Ln = $ Tb to 310 K for $Ln = $ Dy (Table 1). The sharpest transitions are obtained for $Ln = $ Tb and Dy, the resistivity variations at T_{MI} reaching nearly one order of magnitude within 10 K. For $Ln = $ Tb, the $\rho(T)$ curve registered during heating is also shown in the inset of Fig. 7. A clear hysteresis of about 8 K is observed between both cooling and heating curves, suggesting that this transition is of first order. The resistivity values at 400 K (10^{-3}–$10^{-4}\,\Omega$ cm) are typical of metallic oxides and one can also note that the $\rho(400$ K) value gradually increases from $4 \times 10^{-4}\,\Omega$ cm for $Ln = $ Pr to $4 \times 10^{-3}\,\Omega$ cm for $Ln = $ Ho (see also Table 1). Since the highest oxygen contents are observed for the largest lanthanides, it thus seems that the metallicity tends to decrease as the cobalt valency decreases.
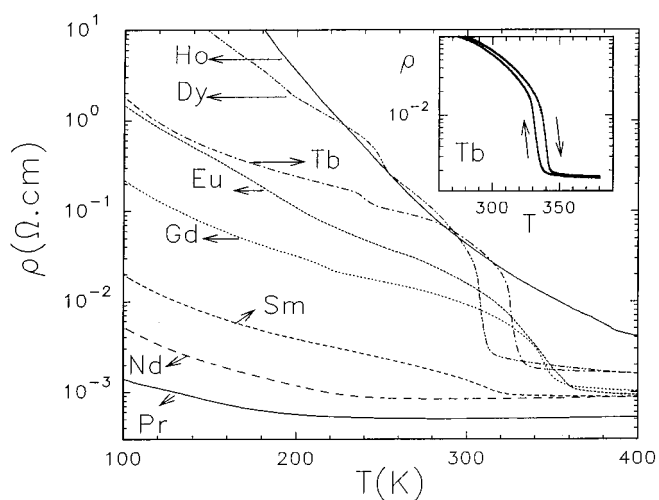

FIG. 8. $\rho(T)$ curves for $GdBaCoO_{5+\delta}$ (air-synthesized (a); argon annealed (b); oxygen-annealed (c)), $HoBaCo_2O_{5+\delta}$ (air-synthesized (d); oxygen-pressure annealed (e)), and $PrBaCo_2O_{5+\delta}$ (air-synthesized (f); argon annealed (g)).

This MI transition is not directly due to the size of the lanthanide but is in fact correlated with the oxygen stoichiometry. This is demonstrated by comparing the $\rho(T)$ curve of the air-synthesized phase $GdBaCo_2O_{5.4}$ (curve a, Fig. 8) with those of the argon-annealed phase $GdBaCo_2O_5$ (curve b, Fig. 8) and oxygen-annealed phase $GdBaCo_2O_{5.6}$ curve c, Fig. 8. It is indeed remarkable that the MI transition is suppressed in the two latter samples. Thus it seems that there exists an optimal carrier doping for the appearance of the MI transition that coincides approximately with the $O_{5.5}$ stoichiometry, characteristic of a cobalt

FIG. 7. T dependence of the resistivity (ρ) for the air-synthesized $LnBaCo_2O_{5+\delta}$ cobaltites. The different Ln are labeled on the graph. Inset: enlargement of the transition ($Ln = $ Tb); the arrows indicate the cooling and heating modes.

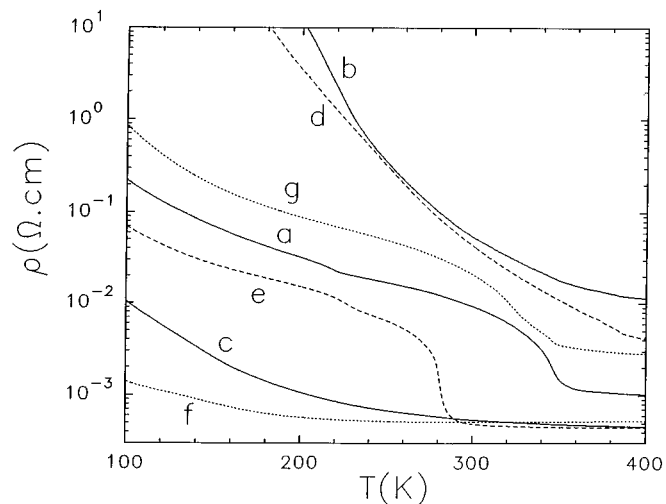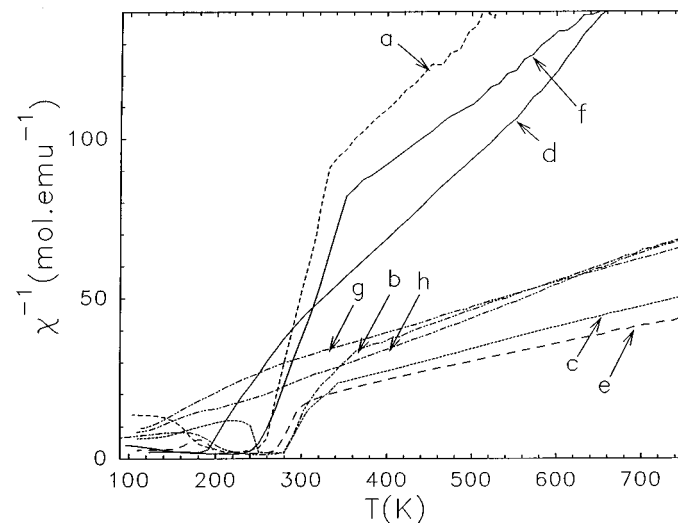**FIG. 9.** T dependence of the inverse of susceptibility (χ^{-1}) for the air-prepared $LnBaCo_2O_{5+\delta}$ samples ($Ln = $ Sm (a), Gd (b), Tb (c), Pr (d), Ho (e)) and annealed samples (argon annealed, $Ln = $ Pr (f) and Gd (g); oxygen annealed, $Ln = $ Gd(h)).

3+ valency. In other words, the O$_5$ composition, which involves mixed divalent and trivalent cobalt would be underdoped, whereas the O$_{5.6}$, which involves mixed trivalent and tetravalent species, would be overdoped. Such a viewpoint is confirmed by the $\rho(T)$ curve of the Ho sample annealed under an oxygen pressure (curve e, Fig. 8), which exhibits a MI transition at 290 K whereas the as-synthesized sample does not (curve d, Fig. 8). Similarly, the MI transition can be restored in the Pr phase by annealing the as-synthesized sample PrBaCo$_2$O$_{5.7}$ (curve f, Fig. 8) in a reduced atmosphere (under argon flow), leading to PrBaCo$_2$O$_{5.5}$ that exhibits a T_{MI} close to 350 K (curve g, Fig. 8).

Magnetic Susceptibility Anomaly at T_{MI}

The reciprocal susceptibility has been plotted versus temperature for all of the compounds of the series. The $\chi^{-1}(T)$ curves are shown in Fig. 9 for several of these phases.

Considering the as-synthesized cobaltites, the following features can be emphasized:

(i) All of the as-synthesized oxides corresponding to intermediate Ln^{3+} size (i.e., Ln = Sm, Eu, Gd, Tb) exhibit an abrupt drop of χ^{-1} as T decreases. Moreover, the temperature of this change of slope coincides with T_{MI}. This is illustrated in Fig. 9 for three compounds, Ln = Sm (curve a), Gd (curve b), and Tb (curve c).

(ii) In contrast, no abrupt variation of the slope of the $\chi^{-1}(T)$ curve is observed for the larger lanthanides Ln = Pr and Nd (curve d, Fig. 9 for Ln = Pr).This behavior is in agreement with the absence of a MI transition for these as-synthesized phases.

(iii) The as-synthesized oxide corresponding to Ln = Ho shows an abrupt drop of χ^{-1} around 300 K (curve e, Fig. 7, for Ln = Ho) although it does not exhibit any MI transition.

The results obtained for the as-synthesized phases corresponding to Ln = Pr, Nd, Sm, Eu, Gd, and Tb suggest that the MI transition seen on the $\rho(T)$ curves (Fig. 7) is in fact related to paramagnetic–ferromagnetic transition that would start below T_{MI}, as shown from the $\chi^{-1}(T)$ curves (Fig. 9). This viewpoint is also supported by the fact that the argon-annealed samples corresponding to Ln = Pr or Nd, characterized by a MI transition, exhibit a drop of χ^{-1} around 300 K as shown for PrBaCo$_2$O$_{5.4}$ (curve f, Fig. 9), contrary to PrBaCo$_2$O$_{5.7}$ (curve d, Fig. 9). The absence of a drop for the Ar-annealed phase GdBaCo$_2$O$_5$ (curve g, Fig. 9), which does not exhibit any MI transition (curve b, Fig. 8), contrary to the air-synthesized oxide GdBaCo$_2$O$_{5.4}$ (curve b, Fig. 9), also supports this viewpoint. No transition is also observed for the oxygen-annealed Gd sample (curve h, Fig. 9). The fact that the as-synthesized Ho sample exhibits a drop in the $\chi^{-1}(T)$ curve but no MI transition from the $\rho(T)$ curve indicates that the paramagnetic to ferromag-

netic transition does not automatically imply a MI transition.

The effective magnetic moments deduced from the high-temperature range of the $\chi^{-1}(T)$ curves vary from 3.1 to 4.5 μ_B/mol of Co. As previously explained for Ln = Gd and Eu, the magnetic anomaly in the $\chi^{-1}(T)$ curve close to T_{MI} observed for as-synthesized oxides Ln = Sm, Eu, Gd, and Tb and argon-annealed phases Ln = Pr and Nd can be interpreted by a spin transition at this temperature. Considering the data previously obtained for LaCoO$_3$ (9), where the trivalent cobalt evolves from high spin (HS, Co^{3+}) to low spin (LS, Co(III)), i.e., from 50 Co^{3+}:50 Co(III) below 350 K to only Co^{3+} at higher temperature, a similar mechanism can be proposed for the ideal composition LnBaCo$_2$O$_{5.5}$. Thus, in those oxides a spin state ordering is most probable below T_{MI}, with Co(III) LS in octahedra and IS Co^{3+} (IS: intermediate spin (4)) in pyramids, both spin states evolving toward Co^{3+} (HS) above T_{MI}. For as-synthesized oxides LnBaCo$_2$O$_{5.3}$ with Ln = Dy and Ho, ordering still exists with Co(III) LS in octahedra, but in that case one can speculate that Co^{2+} will adopt preferentially the pyramidal coordination. The presence of these Co^{2+} species may explain the tendency to electronic localization for HoBaCo$_2$O$_{5.3}$ and consequently the absence of a MI transition.

Evidence for Magnetoresistance Properties

The evolution of the temperature-dependent resistivity in an applied magnetic field of 7 T shows that all of the as-synthesized samples exhibit a negative magnetoresistance at low temperature. This magnetoresistance effect is illustrated for several as-synthesized phases in Fig. 10. For the semiconductors LnBaCo$_2$O$_{5.7}$, with Ln = Pr and Nd, and HoBaCo$_2$O$_{5.3}$, the magnetoresistance (MR) effect appears at low temperature ($T < T_{MR}$), T_{MR} ranging from 150 to 170 K (see, for instance, Fig. 10a for Ln = Pr). For all other as-synthesized oxides which exhibit a MI transition, i.e., for Ln = Sm, Gd, Eu, Tb, and Dy, the MR effect appears at higher temperature, i.e., between 200 and 250 K, but systematically below T_{MI}. The $\rho(T)$ curves under 0 and 7 T indeed merge at T_{MR} = 230 K for Ln = Gd (Fig. 10b), at T_{MR} = 200 K for Ln = Eu (Fig. 10c), and at T_{MR} = 250 K for Ln = Dy (Fig. 10d), whereas the transition temperatures T_{MI} are 350, 360, and 310 K, respectively. Thus the magnetoresistance properties are not simply related to the MI transition. Nevertheless it is worth pointing out that the MR effect is strongly influenced by oxygen content. One indeed observes that the Ar-reduced phase GdBaCo$_2$O$_5$ and the oxygen pressure annealed oxide GdBaCo$_2$O$_{5.6}$, which are both semiconductors, do not exhibit any MR effect, contrary to GdBaCo$_2$O$_{5.4}$ (Fig. 10b). Similarly, the oxygen pressure annealed oxide HoBaCo$_2$O$_{5.5}$, which exhibits a MI transition at 280 K, shows a MR effect $T_{MR} \cong 230$ K (Fig. 10e), i.e., at a higher temperature than the corresponding
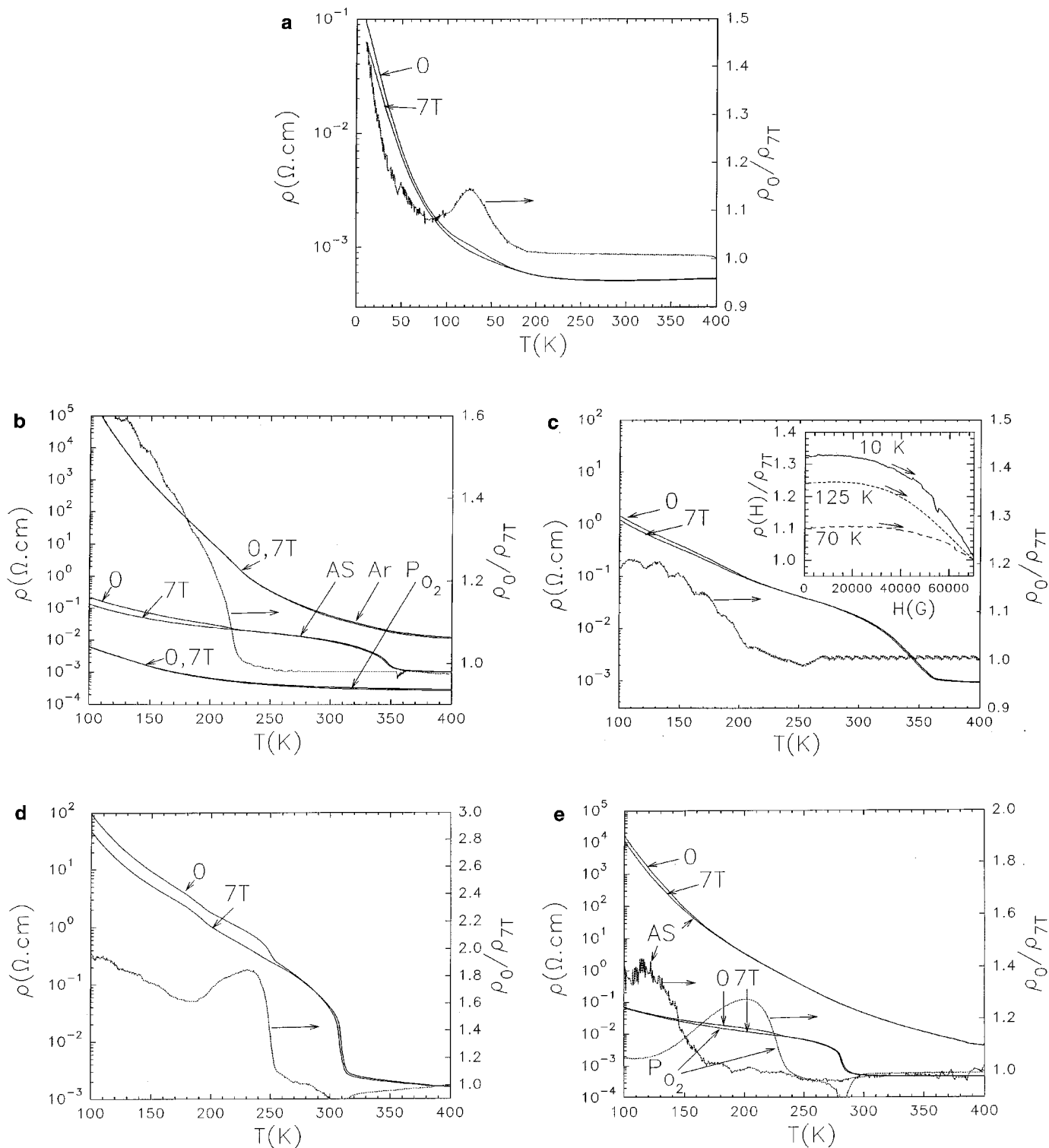
FIG. 10. $\rho(T)$ curves registered at 0 and 7 T by cooling from 400 to 5 K for $LnBaCoO_{5+\delta}$ samples and corresponding T dependence of the resistivity ratio ρ_0/ρ_{7T} (right y-axis): $Ln = $ Pr (a), $Ln = $ Gd (b), $Ln = $ Eu (c), $Ln = $ Dy (d), and $Ln = $ Ho (e). As, Ar, and P_{O_2} are for air-synthesized, Ar annealed (850°C, 15 h), and oxygen-pressure ($P_{O_2} = 100$ bars, 400°C 48 h) annealed, respectively. Isothermal $\rho(H)$ curves are also given for $Ln = $ Eu in the inset of (c).

as-synthesized HoBaCo₂O₅.₃ ($T_{MR} \cong 170$ K), which is semiconductor.

The magnetoresistance of the investigated samples was also probed by measuring $\rho(H)_T$ curves. All of the samples were found to exhibit magnetoresistance percentages (MR% = $(\rho_0 - \rho_{7T})/\rho_0$) values of 10–20% at 125 K (see last line of Table 1). This ratio is even higher at 10 K, reaching 66% for Ln = Gd. Typical $\rho(H)$ curves are given for Ln = Eu in the inset of Fig. 10c. These MR% are comparable to the highest values reported for $La_{1-x}Sr_xCoO_3$ perovskites (3).

Competition between Antiferromagnetism and Ferromagnetism

The existence of a metal to insulator transition as T decreases as well as the evidence for magnetoresistance effect at low temperature emphasizes that the ordered oxygen-deficient perovskites $LnBaCo_2O_{5.5}$ have a similar behavior to the "charge-ordered" manganites $Ln_{1/2}Sr_{1/2}MnO_3$ with Ln = Pr and Nd (10, 11). They differ, however, from the latter by the fact that T_{MR} is much smaller than T_{MI}. In the manganites $Ln_{1/2}Sr_{1/2}MnO_3$, it was clearly evidenced that the MI transition coincides with a transition from a ferromagnetic to an antiferromagnetic state as T decreases. In the case of the cobaltites, the $\chi^{-1}(T)$ curves show a ferromagnetic to an antiferromagnetic transition but the appearance of antiferromagnetism is not so obvious, except that the extrapolation of the high-temperature part of $\chi^{-1}(T)$ to $\chi^{-1} = 0$ leads to a negative θ_p value, indicative of antiferromagnetism. The study of the ac magnetic susceptibility versus temperature allows us to shed light on this issue.

The $\chi'(T)$ curves of the as-synthesized cobaltites, displayed in Fig. 11, show that all of the compounds, from
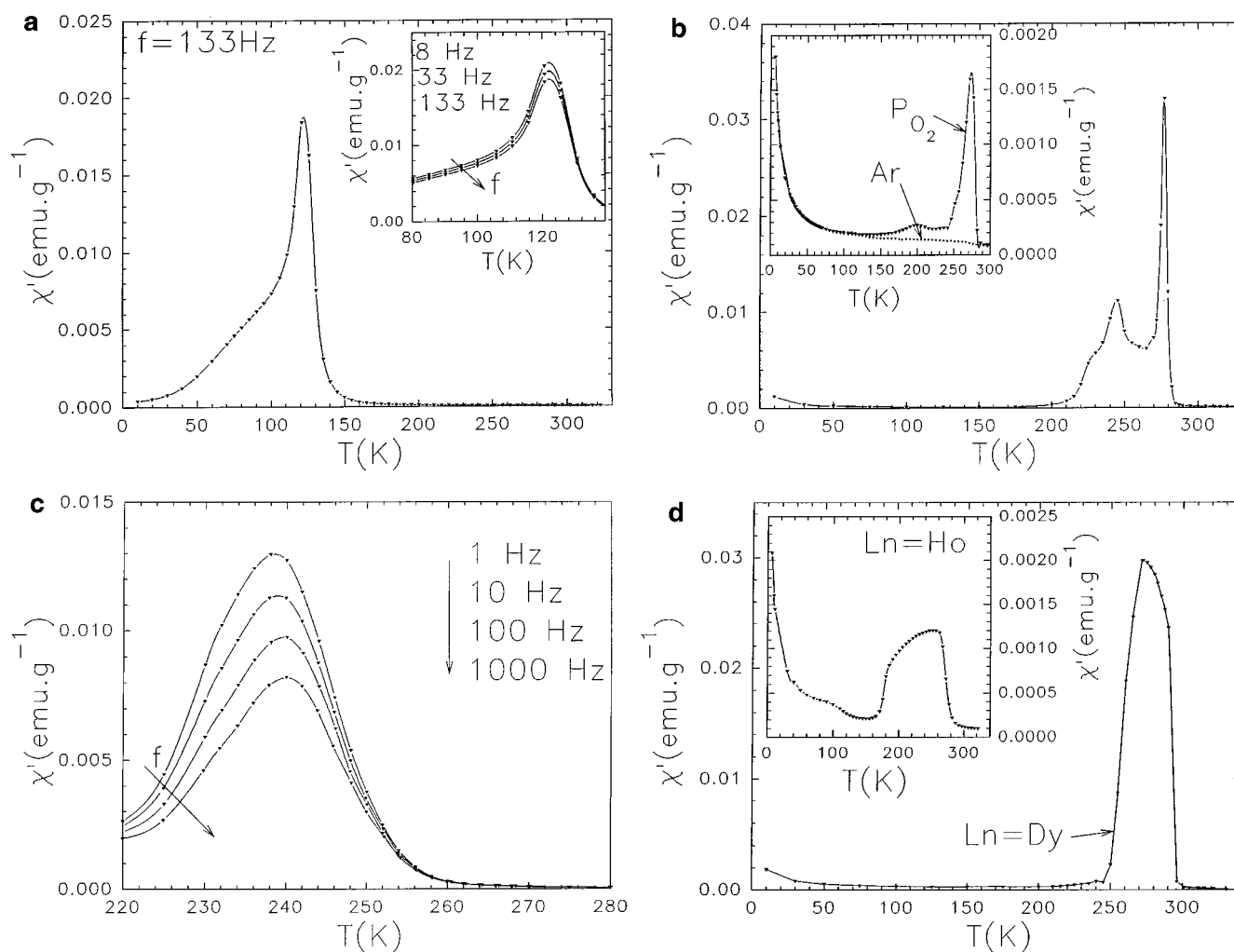

FIG. 11. T dependence of the magnetic susceptibility (real part χ') of the $LnBaCo_2O_{5+\delta}$ samples. (a) Air-prepared Ln = Pr sample; inset: enlargement in the cusp vicinity of the three $\chi'(T)$ curves registered with f = 8, 33, and 113 Hz. (b) Air-synthesized Ln = Gd sample (f = 133 Hz); inset: corresponding curves for the argon (Ar) and oxygen-pressure (P_{O_2}) annealed Ln = Gd samples. (c)Air-prepared Ln = Sm sample; the four $\chi'(T)$ curves from top to bottom correspond to f = 1, 10, 100, and 1000 Hz. (d) Air-prepared Ln = Dy and Ln = Ho (inset) samples.

$Ln = \mathrm{Pr}$ to $Ln = \mathrm{Tb}$, exhibit a cusp which is suggestive of a competition between ferromagnetic and antiferromagnetic interactions. Moreover, the temperature of the cusp T_{cusp} (Table 1), is much smaller for the Pr and Nd phases, for which $T_{\mathrm{cusp}} \cong 105\text{–}120 \, \mathrm{K}$ (see, for instance, Fig. 11a for $Ln = \mathrm{Pr}$), than for $Ln = \mathrm{Sm}$, Eu, Gd, and Tb, for which $T_{\mathrm{cusp}} \cong 275\text{–}240 \, \mathrm{K}$ (see, for instance, Figs. 11b and 11c for $Ln = \mathrm{Gd}$, and Sm, respectively). It is remarkable that T_{cusp} coincides approximately with the appearance of the MR effect, since $T_{\mathrm{MR}} \cong 150\text{–}170 \, \mathrm{K}$ for $Ln = \mathrm{Pr}$ and Nd (Fig. 10a) and $T_{\mathrm{MR}} = 200\text{–}250 \, \mathrm{K}$ for $Ln = \mathrm{Sm}$, Gd, Eu, and Tb (Figs. 10b and 10c). This demonstrates, once again, that the MR effect is closely related to the competition between ferromagnetism and antiferromagnetism.

For the smaller lanthanides, $Ln = \mathrm{Dy}$ and Ho, the as-synthesized oxides $Ln\mathrm{BaCo_2O_{5.3}}$ do not exhibit a sharp cusp on the $\chi^{-1}(T)$ curves, but instead a bell-shaped curve (Fig. 11d). For $Ln = \mathrm{Dy}$ (Fig. 11d), the $\chi'(T)$ curve exhibits indeed two separate magnetic transitions which can be interpreted by the existence of a ferromagnetic component in the 250–300 K range. This kind of curve is rather similar to those of charge-ordered manganites $\mathrm{Pr_{0.5}Sr_{0.5}MnO_3}$ (11), which show two types of magnetic transitions as T decreases, i.e., P–F and F–AF successively. This reinforces our hypothesis of the existence of two types of strong magnetic interactions, ferromagnetic and antiferromagnetic, in these materials. Note also that the temperature for the appearance of ferromagnetism $T \cong 300 \, \mathrm{K}$ (right branch of the curve) is close to $T_{\mathrm{MI}} \cong 310 \, \mathrm{K}$ deduced from the $\rho(T)$ curve, whereas the temperature corresponding to the transition to the AF state $T_{\mathrm{AF}} \cong 250 \, \mathrm{K}$ (left branch of the curve) coincides approximately with $T_{\mathrm{MR}} \cong 250 \, \mathrm{K}$. For $Ln = \mathrm{Ho}$ (inset of Fig. 11d), one still observes two transitions, but the latter are broadened and, above all, the χ' value is strongly reduced (see also Table 1). Thus one can speculate that, in that case, the development of the ferromagnetic component is strongly weakened. The θ_{p} value of $-160 \, \mathrm{K}$ deduced from the $\chi^{-1}(T)$ curve (Fig. 9), which is the smallest value for the 112 series, indicates that the AF interactions dominate. Thus this strong decrease of ferromagnetism is in agreement with the disappearance of the MI transition and of the MR effect.

The effect of the oxygen content upon $\chi'(T)$ corroborates the foregoing statement. Indeed, one observes that for the underdoped sample $\mathrm{GdBaCo_2O_5}$ the cusp on the curve has completely disappeared (inset of Fig. 11b), in agreement with the fact that this argon-annealed phase does not exhibit any magnetoresistance properties nor MI transition. Similarly, for the overdoped sample $\mathrm{GdBaCo_2O_{5.6}}$, which is no longer magnetoresistant, one observes that the intensity of the peak is very weak (inset of Fig. 11b), 20 times smaller than that of the air-synthesized phase $\mathrm{GdBaCo_2O_{5.4}}$ (Fig. 11b).

Finally, it is worth pointing out the particular behavior of the air-synthesized Sm phase $\mathrm{SmBaCo_2O_{5.4}}$. One observes

a frequency dependence of T_{cusp} (Fig. 11c), contrary to the air-synthesized phases with $Ln = \mathrm{Pr}$, Nd, Eu, Gd, and Tb, which also exhibit a cusp on the $\chi'(T)$ curves (see, for instance, inset of Fig. 11a for $Ln = \mathrm{Pr}$). T_{cusp} increases indeed from 238.5 to 240 K as f increases from 1 Hz to 1 kHz and, moreover, these curves merge at a higher temperature ($\sim 260 \, \mathrm{K}$) than that of the cusp ($T = 238.5 \, \mathrm{K}$). Both features are characteristics of spin glass behavior. To check this conclusion, we calculated $K = \Delta T_{\mathrm{cusp}}/[T_{\mathrm{cusp}}(\Delta \ln f)]$ (13). The $K = 2 \times 10^{-3}$ value for $\mathrm{SmBaCo_2O_{5.4}}$ is typical of spin glass values ($\mathrm{CuMn}{:}5 \times 10^{-3}$ (13)) and smaller than the typical values expected for superparamagnets ($a = (\mathrm{Ho_2O_3})(\mathrm{B_2O_3})$: 0.28 (13)). This spin glass-like behavior observed for $Ln = \mathrm{Sm}$ is not unexpected if one considers that samarium is the first cation in the lanthanide series after the oxygen-rich compounds ($Ln = \mathrm{Pr}$, Nd). This may result in a large amount of local disorder between both disordered and ordered structures and since those two kinds of compounds exhibit different magnetic behaviors, one can imagine that magnetic frustrations are favored for $Ln = \mathrm{Sm}$.

Demonstration for the Existence of a Ferromagnetic Component

One crucial feature of the magnetic studies of these 112 phases is the existence of ferromagnetism in the vicinity of T_{cusp} for samples with an oxygen stoichiometry close to $\mathrm{O_{5.5}}$. For this class of compounds corresponding to only trivalent cobalt, it is difficult to anticipate such a magnetic behavior if one refers to the AF interactions existing between cobalt atoms with like spins in perovskite structures. However, the present structural study demonstrates that the structure of these phases is no longer 3D since a 2D character results from the ordering of the oxygen atoms in the $[Ln\mathrm{O}_\delta]_\infty$ layer. In this respect, a possible ordering of LS Co(III) and IS $\mathrm{Co^{3+}}$ in the sixfold and fivefold sites is suspected to be responsible for the magnetic transition occurring at T_{MI}. In the region of this transition a possible canting of the cobalt spins would explain the F component that disappears for $T \ll T_{\mathrm{MI}}$ as shown from the ac–χ curves exhibiting an AF state for these temperatures.

For $Ln = \mathrm{Eu}$, half-hysteresis loops have thus been registered to probe the F component (Fig. 12). One can see that the curves registered for $180 \leq T \leq 270 \, \mathrm{K}$ show a strong hysteretic behavior in the low magnetic field region and especially remanent magnetizations that are indicative of ferromagnetism. Nevertheless, the lack of saturation in large magnetic field (even in 5 T) emphasizes the frustrated nature of the magnetic behavior, in good agreement with the small remanent magnetization of only $10^{-2} \, \mu_{\mathrm{B}}$ at 220 K.

In contrast, for $T \ll T_{\mathrm{cusp}}$ (for instance, $T = 70 \, \mathrm{K}$) the $M(H)$ curves are only straight lines with a very weak hysteresis, in good agreement with antiferromagnetism (not shown). The existence of hysteresis is also shown on
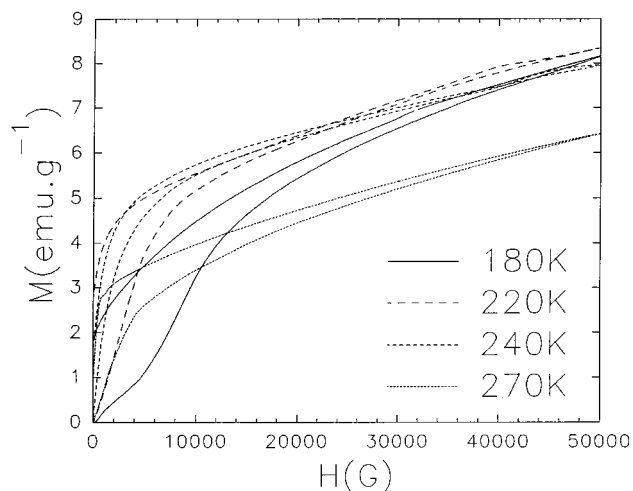
FIG. 12. Isothermal magnetic field dependent magnetization (M) registered for air-prepared EuBaCo$_2$O$_{5+\delta}$. T values are labeled on the graph.

FC–ZFC susceptibility curves registered for different magnetic fields (Fig. 13). One can see on these curves that the FC and ZFC curves merge only for $T > T_{cusp}$ for 10^2 G and that the transition becomes broader for 10^4 G.

Both kinds of $M(H)$ and $M(T)$ curves obviously demonstrate that ferromagnetism develops in the T_{cusp} vicinity.

CONCLUSION

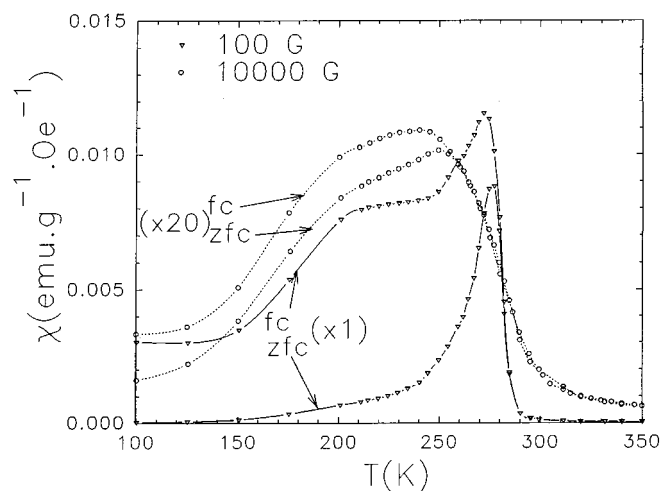This study of different Ln-112 cobaltites demonstrates the important role of the oxygen stoichiometry, itself linked to the lanthanide ionic radius, in both structural ordering and magnetotransport properties. The origin of the MI transition, observed on the resistivity curves in the range $310 \leq T_{MI} \leq 360$ K, correlated with the appearance of a ferromagnetic component (F), is closely related to the O$_{5.5}$ stoichiometry. The existence of trivalent cobalt in an ordered array of pyramids and octahedra suggests a spin transition in these cobaltites at this temperature. Moreover, at a temperature lower than T_{MI}, the resistivity curves start to exhibit a negative magnetoresistance which is related to the establishment of an antiferromagnetic state (AF). Such a magnetic behavior fits perfectly well with the ac–χ behavior, which is characterized by cusps or dome-shaped curves. The competition between both F and AF magnetic states seems to be enhanced for $Ln = $ Sm, whose cusp temperature is frequency dependent, suggesting a spin glass-like behavior. Nevertheless, the existence of a ferromagnetic component in a narrow range of temperatures for these compounds is still to be explained. A possible canting of the spin between cobalt in fivefold and sixfold coordinations may be responsible for this ferromagnetic component; the Ln-112 cobaltites would thus be viewed as ferrimagnets in a restricted T range. Finally, it is remarkable that the structural anisotropy of these cobaltites resulting from the ordering of the oxygen vacancies allows generation of new original magnetotransport properties.

FIG. 13. $\chi(T)$ curves obtained from zfc and fc $M(T)$ curves registered at 10^2 and 10^4 G for the air-prepared EuBaCo$_2$O$_{5+\delta}$ sample. For clarity, the 10^4 G data have been multiplied by 20.

REFERENCES

1. G. Briceno, H. Chang, X, Sun, P. G. Schultz, and X. D. Xiang, *Science* **270,** 273 (1995).
2. S. Yamaguchi, H. Taniguchi, H. Tagagi, T. Arima, and Y. Tokura, *J. Phys. Soc. Jpn.* **64,** 1885 (1995).
3. R. Mahendiran and A. K. Raychaudhuri, *Phys. Rev. B* **54,** 16044 (1996); R. Mahendiran, A. K. Raychaudhuri, A. Chainani, and D. D. Sarma, *J. Phys. Condens. Matter* **7,** 4561 (1995).
4. L. Barbey, N. Nguyen, V. Caignaert, M. Hervieu, and B. Raveau, *Mater. Res. Bull.* **27,** 295 (1992); L. Barbey, N. Nguyen, V. Caignaert, F. Studer, and B. Raveau, *J. Solid State Chem.* **112,** 148 (1994).
5. C. Martin, A. Maignan, D. Pelloquin, N. Nguyen, and B. Raveau, *Appl. Phys. Lett.* **71,** 1421 (1997).
6. L. Er-Rakho, C. Michel, Ph. Lacorre, and B. Raveau, *J. Solid State Chem.* **73,** 531 (1988); V. Caignaert, I. Mirebeau, F. Bourée, N. Nguyen, A. Ducouret, J. M. Grenèche, and B. Raveau, *J. Solid State Chem.* **114,** 24 (1995).
7. J. Rodriguez-Carvajal, *in* "Collected Abstracts of Powder Diffraction Meeting" (J. Galy, Ed.), p. 127, Toulouse, France, 1990.
8. W. Zhou, *Chem. Mater.* **6,** 441 (1994); W. Zhou, C. T. Lin, and W. Y. Liang, *Adv. Mater.* **5,** 735 (1993).
9. M. A. Senaris-Rodriguez and J. B. Goodenough, *J. Solid State Chem.* **118,** 323 (1995).

10. H. Kuwahara, Y. Tomioka, A. Asamitsu, Y. Moritomo, and Y. Tokura, *Science* **270,** 961 (1995); V. Caignaert, F. Millange, M. Hervieu, E. Suard, and B. Raveau, *Solid State Commun.* **99,** 173 (1996).

11. Y. Tomioka, A. Asamitsu, Y. Moritomo, H. Kuwahara, and Y. Tokura, *Phys. Rev. Lett.* **74,** 5108 (1995); H. Kawano, R. Kajimoto, M. Yoshizawa, Y. Tomioka, H. Kuwahara, and Y. Tokura, *Phys. Rev. Lett.* **78,** 4253 (1997); D. N. Argyriou, D. G. Hinks, J. F. Mitchell, C. D. Potter, A. J. Schultz, D. M. Young, J. D. Jorgensen, and S. D. Bader, *J. Solid. State Chem.* **124,** 381 (1996).

12. R. D. Shannon, *Acta Crystallogr. Sect. A* **32,** 751 (1976).

13. J. A. Mydosh, "Spin glasses." Taylor & Francis, London, Washington, DC, 1993.